atoms

MDPI

Article

Orbital Angular Momentum-Resolved Photon Channels for Tailoring High-Harmonic Generation in Bichromatic Vortex Fields

Zi-Jian Xiang [1], Rui-Yuan Zhang [1] and Jing Guo [2,*]

[1] College of Physics, Jilin University, Changchun 130012, China; xiangzj1123@mails.jlu.edu.cn (Z.-J.X.); zhangry1123@mails.jlu.edu.cn (R.-Y.Z.)
[2] Institute of Atomic and Molecular Physics, Jilin University, Changchun 130012, China
* Correspondence: gjing@jlu.edu.cn

Abstract

Tailoring the spatial and angular-momentum structure of high-harmonic radiation is an important route toward controllable extreme-ultraviolet structured light. Here, we introduce an orbital angular momentum (OAM)-resolved photon-channel framework to elucidate spatial-mode formation in high-harmonic generation driven by bichromatic vortex fields. Combined with numerical solutions of the time-dependent Schrödinger equation for argon, this framework shows that the spatial structure of the emitted harmonics is governed by spectral broadening and interference among dominant OAM-carrying photon channels. This mechanism drives a continuous transition from clean vortex beams at harmonic peaks, characterized by high OAM purity, nearly pure circular polarization, and strong transverse coherence, to disordered speckle-like patterns in harmonic valleys, where multi-channel interference induces pronounced phase distortion. These results identify photon-channel interference as a useful mechanism for controlling the OAM, polarization, and spatial coherence of harmonic beams. The proposed analysis provides a field-control and OAM-channel framework that may be extended in future studies to structured-light probes of ultrafast dynamics and topological phases in quantum materials.

Keywords: high-harmonic generation; orbital angular momentum; photon channel; vortex beam; structured light; bichromatic field

1. Introduction

High-order harmonic generation (HHG) is a central topic in strong-field physics and attosecond science. Early experiments by McPherson et al. [1] and Ferray et al. [2] reported the generation of odd harmonics from rare gases. The semiclassical three-step model proposed by Corkum [3] provided an intuitive picture of HHG in terms of tunnel ionization, laser-driven acceleration, and electron–ion recombination. This framework led to major experimental advances, including the generation of isolated attosecond pulses by Hentschel et al. [4], which established the foundation of attosecond metrology.

With the development of laser technology, multicolor driving fields have become an important tool for controlling HHG. Mauritsson et al. [5] showed that two-color laser fields break inversion symmetry and enable the generation of both odd and even harmonics. Building on this idea, Bertrand et al. [6] investigated the wave-mixing character of HHG in the spatial domain. By superposing a strong fundamental field with a weak second-harmonic field in a noncollinear geometry, they spatially separated harmonics generated

Check for updates

Academic Editors: Jean-Patrick Connerade and Emmanouil Benis

Received: 30 March 2026
Revised: 23 June 2026
Accepted: 11 July 2026
Published: 22 July 2026

Copyright: © 2026 by the authors. Licensee MDPI, Basel, Switzerland. This article is an open access article distributed under the terms and conditions of the Creative Commons Attribution (CC BY) license.

through different photon-number combinations (n_1, n_2). They further showed that the harmonic yield scales perturbatively with the weak-field intensity as $I_2^{n_2}$, linking nonperturbative HHG with perturbative nonlinear optics and suggesting a photon-exchange picture.

To interpret these observations, Li et al. [7] proposed the photon-channel theory, in which both the driving fields and the emitted harmonic field are quantized. Within this framework, HHG is described as a quantum process in which an atom absorbs specific numbers of driving-field photons and emits a single high-energy photon. The theory provides an analytical expression for the contribution of each channel, thereby explaining channel competition and intensity-scaling laws and extending HHG to a fully quantized description.

Recent research has further expanded HHG into optical fields with complex spatiotemporal structures, especially vortex beams carrying OAM. The modern understanding of OAM in light beams originates from Allen et al. [8], who showed that Laguerre–Gaussian (LG) beams carry OAM independently of spin angular momentum. In vortex-driven HHG, the relevant conservation laws extend beyond energy and linear momentum to include OAM. Zürch et al. [9] used vortex beams to generate high-order harmonics. Hernández-García et al. [10] theoretically proposed attosecond vortex pulses and established a relation between the OAM of the driving field and that of the emitted harmonics. Gariepy et al. [11] experimentally demonstrated OAM control in HHG and confirmed angular momentum conservation. Subsequent studies by Géneaux et al. [12], Kong et al. [13], and Gauthier et al. [14] further advanced the generation and control of vortex harmonics.

More recently, efforts have begun to connect the photon-channel picture with OAM conservation. For example, Wang et al. [15] showed that, in two-color vortex-driven HHG, different photon channels imprint distinct OAM values onto the emitted harmonics, enabling channel selection through intensity tuning. This result established a direct connection between microscopic quantum pathways and the topological charge of harmonic vortices. Nevertheless, a comprehensive framework that incorporates OAM as an intrinsic degree of freedom into the quantized photon-channel description is still lacking.

In this work, we develop an OAM-resolved photon-channel formalism for high-order harmonic generation. In this framework, photon pathways are identified not only by the numbers of absorbed photons, but also by the OAM quantum numbers carried by the participating fields, consistent with angular-momentum selection rules. We further establish a direct connection between this theoretical picture and experimentally accessible observables. In particular, we show that the complex intensity distributions and helical phase structures of the harmonics can be understood as spatial manifestations of interference among OAM-carrying photon channels with finite spectral bandwidths. Using this framework, we simulate and interpret the evolution of harmonic spatial modes, and discuss its implications for controlling harmonic OAM, polarization, and spatial coherence, as well as its possible future extension to topological materials.

2. Theoretical Methods

This work employs numerical solutions of the time-dependent Schrödinger equation (TDSE) to simulate HHG from Ar atoms driven by bichromatic LG vortex fields. The method combines model atomic potentials, a transverse LG description of the driving field, local TDSE calculations on a two-dimensional electronic grid, and post-processing of the complex harmonic near field. The emitted harmonics are analyzed in terms of their spatial intensity and phase distributions, polarization states, OAM spectra, effective transverse phase mismatch, transverse coherence length, and far-field propagation.

2.1. Numerical Method for Solving the TDSE

To simulate HHG from Ar atoms driven by vortex laser fields, we numerically solve the TDSE,

$$i\frac{\partial}{\partial t}\psi(\mathbf{r},t;\mathbf{R}) = H(\mathbf{R},\mathbf{r},t)\psi(\mathbf{r},t;\mathbf{R}), \tag{1}$$

where $\mathbf{r} = (x, y)$ is the two-dimensional electronic coordinate used in the reduced TDSE calculation and $\mathbf{R} = (X, Y)$ denotes the transverse coordinate of the macroscopic driving field. The Hamiltonian is

$$H(\mathbf{R},\mathbf{r},t) = T(\mathbf{r}) + V(\mathbf{r}) + V_I(\mathbf{R},\mathbf{r},t), \tag{2}$$

with the length–gauge interaction

$$V_I(\mathbf{R},\mathbf{r},t) = xE_x(\mathbf{R},t) + yE_y(\mathbf{R},t). \tag{3}$$

for each transverse position $\mathbf{R}$, the local value of the structured laser field is inserted into Equation (3), and the TDSE is solved independently.

For argon, we employ two model potentials corresponding to the 3*s* state and to the current-carrying 3*p* state. For the 3*s* state, we use

$$V_{\mathrm{Ar}}^{(3s)}(r) = -\frac{Z}{\sqrt{r^2+\alpha_0}}, \qquad r = \sqrt{x^2+y^2}, \tag{4}$$

where $\alpha_0 = 0.3844$. For the 3*p* state, we use

$$V_{\mathrm{Ar}}^{(3p)}(x,y) = -\frac{Z + Z_{\mathrm{eff}}\exp(-r^2)}{\sqrt{r^2+\alpha_1}}, \tag{5}$$

with $Z = 1$, $Z_{\mathrm{eff}} = 9$, and $\alpha_1 = 3.6$. These are two-dimensional soft-core model potentials with radial symmetry in the simulation plane, not full three-dimensional spherical atomic potentials. The current-carrying state is taken as the $(3p, m = +1)$ state, denoted by p_+, and is constructed as

$$p_+ = \frac{1}{\sqrt{2}}(p_x + ip_y). \tag{6}$$

The TDSE is solved with the split-operator method [16]. The electronic wave function is represented in a two-dimensional box of length 256 a.u. with 512 grid points along both the x and y directions. The time step is $\Delta t = 0.135$ a.u. An absorbing boundary mask is applied near the edges of the electronic grid to suppress unphysical reflections. The time-dependent dipole acceleration is evaluated as

$$a_\alpha(\mathbf{R},t) = \left\langle \psi(t;\mathbf{R}) \middle| -\frac{\partial V}{\partial \alpha} \middle| \psi(t;\mathbf{R}) \right\rangle, \qquad \alpha = x, y. \tag{7}$$

The complex harmonic near-field components are obtained by Fourier transforming the dipole acceleration,

$$\widetilde{E}_{h,\alpha}(\mathbf{R},\Omega) = \int a_\alpha(\mathbf{R},t)W(t)\exp(-i\Omega t)\,dt, \qquad \alpha = x, y, \tag{8}$$

where $W(t)$ is a smooth temporal window. The spectral order is defined as $N_\Omega = \Omega/\omega_1$.

2.2. Laguerre–Gaussian Bichromatic Driving Fields

The transverse profile of each driving-frequency component is generated from an LG mode under the paraxial approximation. The complex LG field used in the numerical preprocessing is written as [17]

$$U_{\ell,p}^{(j)}(r,\theta,z') = E_{0,j}\frac{w_0}{w_j(z')}\left(\frac{r}{w_j(z')}\right)^{|\ell_j|} L_p^{|\ell_j|}\left(\frac{2r^2}{w_j^2(z')}\right)\exp\left[-\frac{r^2}{w_j^2(z')}\right] \times \exp\left[-i\left(\ell_j\theta + k_j\frac{r^2}{2R_j(z')} + \zeta_j(z')\right)\right]. \tag{9}$$

Here, the superscript j labels the driving-frequency component. $E_{0,j} = \sqrt{2I_{0,j}/(c\epsilon_0)}$ is the peak electric-field amplitude of component j, w_0 is the beam waist, $w_j(z') = w_0\sqrt{1+(z'/z_{R,j})^2}$ is the beam radius, $z_{R,j} = \pi w_0^2/\lambda_j$ is the Rayleigh range, and $k_j = 2\pi/\lambda_j = \omega_j/c$. $L_p^{|\ell_j|}$ denotes the associated Laguerre polynomial, ℓ_j is the topological charge of component j, p is the radial index, $R_j(z') = z'[1+(z_{R,j}/z')^2]$ is the wavefront curvature radius, and $\zeta_j(z') = (2p+|\ell_j|+1)\arctan(z'/z_{R,j})$ is the Gouy-phase contribution in the phase convention of Equation (9). The coordinate z' is the longitudinal coordinate used only to generate the paraxial LG profile near the focus. In the present local-source calculation it is sampled in the interval specified below and is not followed by a laboratory-frame gas-propagation transformation. For the two-color fields considered here, the wavelength-dependent quantities k_j, $z_{R,j}$, $w_j(z')$, $R_j(z')$, and $\zeta_j(z')$ are evaluated separately for each frequency component.

Each complex field $U_{\ell,p}^{(j)}$ is converted into the spatially dependent electric-field amplitude and phase supplied to the TDSE calculation. Specifically,

$$I_{\mathrm{LG},j}(\mathbf{R}) = |U_{\ell,p}^{(j)}(X,Y,z')|^2, \qquad \mathcal{E}_{\mathrm{LG},j}(\mathbf{R}) = \sqrt{\frac{I_{\mathrm{LG},j}(\mathbf{R})}{I_{\mathrm{au}}}}, \qquad \Phi_j(\mathbf{R}) = \arg[U_{\ell,p}^{(j)}(X,Y,z')], \tag{10}$$

where $I_{\mathrm{au}} = 3.5\times10^{16}\,\mathrm{W/cm^2}$. The field is normalized such that the maximum LG intensity of each component corresponds to its prescribed peak intensity, after which the converted electric-field amplitudes $\mathcal{E}_{\mathrm{LG},j}$ and phases Φ_j are stored and used as the spatial input for the TDSE simulation. This construction is the way in which the LG mode enters the actual local TDSE calculations.

For the linearly polarized nondegenerate bichromatic field, the local driving field is

$$E_x(\mathbf{R},t) = f(t)\Big[(1-p_2)\mathcal{E}_{\mathrm{LG},1}(\mathbf{R})\cos(\omega_1 t + \Phi_1(\mathbf{R})) + p_2\mathcal{E}_{\mathrm{LG},2}(\mathbf{R})\cos(\omega_2 t + \Phi_2(\mathbf{R}))\Big], \tag{11}$$

$$E_y(\mathbf{R},t) = 0, \tag{12}$$

where $\omega_2 = \kappa\omega_1$ with $\kappa = 1.9$. The dimensionless amplitude-weight factor p_2 controls the relative contribution of the second color in the linearly polarized nondegenerate field; in this work the same value as in the numerical simulations is used for all transverse positions. In Equations (11) and (12), the two temporal components are multiplied by their own frequency-dependent LG amplitudes and phases, $\mathcal{E}_{\mathrm{LG},1}, \Phi_1$ and $\mathcal{E}_{\mathrm{LG},2}, \Phi_2$, respectively.

For the counter-rotating bicircular vortex field with a $\omega_1 : 2\omega_1$ frequency ratio, the frequency-dependent LG amplitudes and phases are explicitly included in the two Cartesian components used in the TDSE:

$$E_x(\mathbf{R},t) = f(t)[\mathcal{E}_{\mathrm{LG},1}(\mathbf{R})\cos(\omega_1 t + \Phi_1(\mathbf{R})) + \mathcal{E}_{\mathrm{LG},2}(\mathbf{R})\cos(2\omega_1 t + \Phi_2(\mathbf{R}))], \tag{13}$$

$$E_y(\mathbf{R},t) = f(t)[\mathcal{E}_{\mathrm{LG},1}(\mathbf{R})\sin(\omega_1 t + \Phi_1(\mathbf{R})) - \mathcal{E}_{\mathrm{LG},2}(\mathbf{R})\sin(2\omega_1 t + \Phi_2(\mathbf{R}))]. \quad (14)$$

The opposite signs of the sine terms define the opposite circular helicities of the two colors. Thus, the bicircular field combines spatial LG factors, temporal oscillations, and circular polarization vectors at the level of the real Cartesian field components used in the TDSE.

The temporal envelope is

$$f(t) = \sin^2\left(\frac{\omega_1 t}{2n}\right), \quad (15)$$

where n is the number of optical cycles. In this work, $\omega_1 = 0.057$ a.u., corresponding to $\lambda_1 = 800$ nm. For the linearly polarized nondegenerate field, $\omega_2 = 1.9\omega_1$ and $\lambda_2 = \lambda_1/1.9$; for the counter-rotating bicircular field, $\omega_2 = 2\omega_1$ and $\lambda_2 = \lambda_1/2$. The total pulse duration is 10 optical cycles. Both driving components use an LG mode with $\ell_1 = \ell_2 = 1$ and $p = 0$, with beam waist $w_0 = 25$ μm. The transverse coordinates are sampled over $X, Y \in [-60\ \mu\mathrm{m}, 60\ \mu\mathrm{m}]$ using a 64×64 grid, and the near-focus longitudinal coordinate used to generate the LG profiles is sampled over $z' \in [0, 1 \times 10^{-9}\ \mathrm{m}]$.

2.3. Photon-Channel Labeling and Geometric Phase Factor

In a nondegenerate bichromatic field, the emitted frequency and the OAM transferred to the harmonic must be distinguished. A photon channel is labeled by (n_1, n_2), where n_1 and n_2 are the numbers of photons absorbed from the two driving components. Energy conservation gives

$$\Omega_{n_1,n_2} = n_1\omega_1 + n_2\omega_2 = (n_1 + \kappa n_2)\omega_1, \quad (16)$$

so that the spectral order is $N_\Omega = n_1 + \kappa n_2$. OAM conservation, by contrast, gives

$$\ell_{n_1,n_2} = n_1\ell_1 + n_2\ell_2. \quad (17)$$

Because both components in the present calculation carry the same LG charge, $\ell_1 = \ell_2 = 1$, the OAM charge associated with a channel is

$$q_{\mathrm{ch}} = n_1 + n_2, \quad (18)$$

even though the emitted spectral order is $N_\Omega = n_1 + \kappa n_2$. For example, in the linearly polarized ω_1–$1.9\omega_1$ case, the channel $(1, 6)$ emits at $N_\Omega = 1 + 1.9 \times 6 = 12.4$ but carries $q_{\mathrm{ch}} = 7$, corresponding to the OAM charge $\ell = 7$ for $\ell_1 = \ell_2 = 1$.

2.4. Phase Mismatch and Transverse Coherence Length

Phase matching in HHG is determined by the coherent buildup of the harmonic field emitted from different spatial positions in the nonlinear medium. In the general macroscopic picture, the phase front of the newly generated nonlinear source should match that of the propagating harmonic field [18]. For HHG driven by a Laguerre–Gaussian beam, Jin et al. further showed that the phase-matching condition can be written in terms of the harmonic wave vector, the driving-field wave vector, and the intensity-dependent dipole-phase contribution as [17]

$$\mathbf{k}_q = q\mathbf{k}_1 + \mathbf{K}, \quad (19)$$

where $\mathbf{k}_q$ is the wave vector of the qth harmonic, $\mathbf{k}_1$ is the local wave vector of the driving LG field, and $\mathbf{K} = \nabla\phi_{\mathrm{dip}}$ represents the contribution from the intrinsic dipole phase. In a full propagation treatment, the phase mismatch may therefore be expressed in vector form as

$$\Delta k = \left|\mathbf{k}_q - (q\mathbf{k}_1 + \mathbf{K})\right|, \quad (20)$$

or, under the forward-propagation approximation used in previous LG-HHG phase-matching analyses, by comparing the magnitude of the harmonic wave vector with that of the source wave vector [17]. The corresponding macroscopic coherence length is commonly defined as $L_{\mathrm{coh}} = \pi/|\Delta k|$.

The present work does not solve the Maxwell propagation equation in a gas medium. Instead, we use the TDSE to obtain the local microscopic harmonic response at each transverse position of the driving vortex field and then analyze the source-plane transverse phase compatibility. For this purpose, we introduce an effective transverse phase mismatch by comparing the calculated harmonic phase with the channel-dependent LG geometric phase. The harmonic phase is extracted from the complex near-field harmonic component as

$$\phi_h(\mathbf{R}, \Omega) = \arg\left[\widetilde{E}_{h,x}(\mathbf{R}, \Omega)\right], \tag{21}$$

where $\mathbf{R} = (X, Y)$ is the transverse coordinate. The phase is unwrapped in the transverse plane before spatial derivatives are evaluated.

For a bichromatic vortex field, the geometric phase factor is determined by the LG phase accumulated from the absorbed photons rather than directly by the emitted spectral order. With frequency-dependent LG modes, the channel phase is $n_1\Phi_1(\mathbf{R}) + n_2\Phi_2(\mathbf{R})$. The residual transverse phase is therefore defined as

$$\Delta\phi_\perp(\mathbf{R}, \Omega) = n_1\Phi_1(\mathbf{R}) + n_2\Phi_2(\mathbf{R}) - \phi_h(\mathbf{R}, \Omega), \tag{22}$$

where $\Phi_1(\mathbf{R})$ and $\Phi_2(\mathbf{R})$ are the frequency-dependent LG phases of the two driving components. This sign convention follows the numerical implementation used in the phase-mismatch analysis; reversing the sign would not change the magnitude of the transverse wave–vector mismatch or the coherence length.

The effective transverse wave–vector mismatch is then evaluated as the magnitude of the transverse gradient of the residual phase,

$$\Delta k_\perp(\mathbf{R}, \Omega) = |\nabla_\perp \Delta\phi_\perp(\mathbf{R}, \Omega)| = \sqrt{\left(\frac{\partial \Delta\phi_\perp}{\partial X}\right)^2 + \left(\frac{\partial \Delta\phi_\perp}{\partial Y}\right)^2}. \tag{23}$$

The corresponding transverse coherence length is defined as

$$L_{\mathrm{coh}}^{\perp}(\mathbf{R}, \Omega) = \frac{\pi}{\Delta k_\perp(\mathbf{R}, \Omega)}. \tag{24}$$

In the numerical implementation, ϕ_h is first obtained from the complex x-polarized harmonic field and then unwrapped on the 64×64 transverse grid. The residual phase in Equation (22) is folded into the interval $[-\pi, \pi]$, and $\Delta k_\perp$ is calculated by central finite differences along the X and Y directions. To avoid artificial divergence in nearly phase-matched regions, we use the cutoff

$$L_{\mathrm{coh}}^{\perp} = \begin{cases} \pi/\Delta k_\perp, & \Delta k_\perp > 10^{-10}\ \text{a.u.}^{-1}, \\ 10^{10}\ \text{a.u.}, & \Delta k_\perp \le 10^{-10}\ \text{a.u.}^{-1}. \end{cases} \tag{25}$$

Boundary values are copied from the nearest interior grid points.

This transverse coherence length should not be interpreted as the full macroscopic longitudinal coherence length of a gas target. Rather, it provides a local diagnostic of how well the TDSE-calculated harmonic phase follows the channel-dependent LG geometric phase at the source plane. Large $L_{\mathrm{coh}}^{\perp}$ indicates a slowly varying residual phase and therefore a spatially coherent harmonic mode, whereas small $L_{\mathrm{coh}}^{\perp}$ indicates rapid transverse

phase variation caused by channel interference and is associated with fragmented or speckle-like spatial structures.

2.5. Stokes Parameters and Polarization States

The polarization state of the harmonic near field is evaluated from the complex harmonic components $\widetilde{E}_{h,x}$ and $\widetilde{E}_{h,y}$. The local Stokes parameters are

$$\begin{aligned} S_0 &= |\widetilde{E}_{h,x}|^2 + |\widetilde{E}_{h,y}|^2, \\ S_1 &= |\widetilde{E}_{h,x}|^2 - |\widetilde{E}_{h,y}|^2, \\ S_2 &= 2\,\mathrm{Re}(\widetilde{E}^*_{h,x}\widetilde{E}_{h,y}), \\ S_3 &= 2\,\mathrm{Im}(\widetilde{E}^*_{h,x}\widetilde{E}_{h,y}). \end{aligned} \tag{26}$$

From these quantities, the local degree of polarization and the normalized circularity are calculated as

$$\mathrm{DoP} = \frac{\sqrt{S_1^2 + S_2^2 + S_3^2}}{S_0}, \qquad \epsilon = \frac{S_3}{\sqrt{S_1^2 + S_2^2 + S_3^2}}. \tag{27}$$

2.6. OAM Spectrum Analysis

For selected harmonic frequencies, the OAM spectrum is obtained from an angular Fourier decomposition of the complex harmonic field. The circular components are constructed as

$$\widetilde{E}_{\mathrm{LCP}} = \widetilde{E}_{h,x} + i\widetilde{E}_{h,y}, \qquad \widetilde{E}_{\mathrm{RCP}} = \widetilde{E}_{h,x} - i\widetilde{E}_{h,y}, \tag{28}$$

and the linearly combined component used only for comparison is $\widetilde{E}_{\mathrm{linear}} = \widetilde{E}_{h,x} + \widetilde{E}_{h,y}$; this post-processing combination should not be confused with the linearly polarized driving field defined in Equations (11) and (12). For any selected complex field $\widetilde{E}(\rho, \varphi, \Omega)$,

$$\widetilde{E}(\rho, \varphi, \Omega) = \sum_{m=-\infty}^{+\infty} \widetilde{E}_m(\rho, \Omega) e^{im\varphi}, \qquad \widetilde{E}_m(\rho, \Omega) = \frac{1}{2\pi} \int_0^{2\pi} \widetilde{E}(\rho, \varphi, \Omega) e^{-im\varphi}\, d\varphi. \tag{29}$$

For N_φ equally spaced angular samples, this integral is evaluated by discrete Fourier summation. The modal intensity and normalized modal weight are

$$L_m(\Omega) = \int_0^{\rho_{\max}} |\widetilde{E}_m(\rho, \Omega)|^2 \rho\, d\rho, \qquad P_m(\Omega) = \frac{L_m(\Omega)}{\sum_m L_m(\Omega)}. \tag{30}$$

In the numerical implementation used for the OAM-spectrum analysis, the Cartesian near-field data are interpolated to a polar grid with $N_\varphi = 360$ angular samples and 100 radial sampling points. The OAM spectrum is evaluated over $m = -15, -14, \ldots, 14, 15$, and the radial integration is performed over the inscribed transverse region available from the 64×64 source grid. The normalized weight P_m is therefore the fraction of the integrated modal intensity carried by mode m within this analyzed range, and the dominant-mode fraction is evaluated as $P_{m_0} = \max_m P_m$. These settings follow the angular Fourier-transform procedure used in the supplied OAM-analysis program, where the number of analyzed modes is 31, and are sufficient to cover the dominant modes observed in the selected harmonics.

2.7. Far-Field Harmonic Emission

To investigate the spatial structure of the harmonic radiation after propagation, the near-field harmonic emission at the exit plane is propagated to the detector plane. In the

numerical implementation, the far-field electric field is obtained from a scalar Huygens-type propagation integral with a spherical-wave kernel,

$$E^{f}_{h,\alpha}(x_f, y_f, z_f, \Omega) = \frac{1}{i\lambda_h} \iint E_{h,\alpha}(x, y, z_{\text{out}}, \Omega) \frac{\exp\left[ik_h R(x, y; x_f, y_f)\right]}{R(x, y; x_f, y_f)}\, dx\, dy, \qquad \alpha = x, y, \tag{31}$$

where

$$R(x, y; x_f, y_f) = \sqrt{(x_f - x)^2 + (y_f - y)^2 + (z_f - z_{\text{out}})^2}, \qquad k_h = \frac{\Omega}{c}, \qquad \lambda_h = \frac{2\pi}{k_h}. \tag{32}$$

Here, (x_f, y_f) are the transverse detector coordinates, $z_f - z_{\text{out}}$ is the propagation distance from the exit plane to the detector plane, and $\alpha = x, y$ denotes the Cartesian polarization component.

3. Results and Discussion

3.1. Harmonic Spectra and Spatial Modes in a Linearly Polarized Bichromatic Vortex Field

Figure 1 shows the initial wave functions of argon used in our simulations. Panels (a) and (b) display the degenerate p_x and p_y orbitals, respectively, both exhibiting the characteristic dipolar dumbbell structure. To construct the initial current-carrying state p_+, we use the normalized coherent superposition defined in Equation (6), as shown in panel (c). This superposition converts the anisotropic dipolar density into a cylindrically symmetric toroidal distribution and introduces a phase singularity at the center, corresponding to nonzero orbital angular momentum and a well-defined azimuthal probability current. Such a construction is physically well-motivated: Eckart et al. [19] experimentally demonstrated the ultrafast preparation and detection of ring currents in argon ions via m-selective tunnel ionization, showing that electrons counter-rotating with respect to the laser field are preferentially removed and leave the residual ion in a state with a definite circulation direction. Their results provide direct experimental evidence that laser-driven ionization can prepare chiral bound states carrying persistent current, which supports the use of the present p_+ state as the initial current-carrying state for studying current-induced HHG dynamics. Panel (d) shows the isotropic distribution of the 3s state calculated using the Coulomb model potential in Equation (4).

Figure 2 presents the HHG spectra from argon atoms driven by a linearly polarized bichromatic vortex field. For a single-color driving field, the harmonic cutoff can be estimated from the semiclassical law [3]

$$E_{\text{cutoff}} = I_p + 3.17U_p, \tag{33}$$

where $I_p = 0.579$ a.u. is the ionization potential of argon and $U_p = E^2/(4\omega^2)$ is the ponderomotive energy. When the two driving components are considered separately as single-color reference fields, the corresponding cutoff orders are approximately 10.9 and 13.4. In the bichromatic case, however, the electron motion is driven by the superposed field, so the cutoff is determined by the maximum recollision energy supported by the composite trajectory rather than by either component individually. From this perspective, an effective cutoff around the 14th order is reasonable. Indeed, Figure 2a shows a pronounced intensity drop beyond harmonic order 14.

The linearly polarized nondegenerate bichromatic vortex field already reveals that the spatial mode of a given harmonic is governed by the competition and interference between neighboring photon channels carrying distinct OAM. Within harmonic orders 11–14, we focus on three representative frequencies: the peak at 12.4, the shoulder at 12.6, and the valley at 12.9. As shown in Figure 3a–c, the near-field intensity evolves

from an ordered annular double-lobe structure with seven spiral arms at the peak, to an asymmetric double-lobe at the shoulder, and finally to a fragmented four-lobe pattern at the valley. The corresponding phase maps in Figure 3e–g show a parallel evolution from a well-defined spiral wavefront to a distorted and ultimately disordered phase structure. This behavior indicates a gradual transition from single-channel-dominated emission to multi-channel interference.

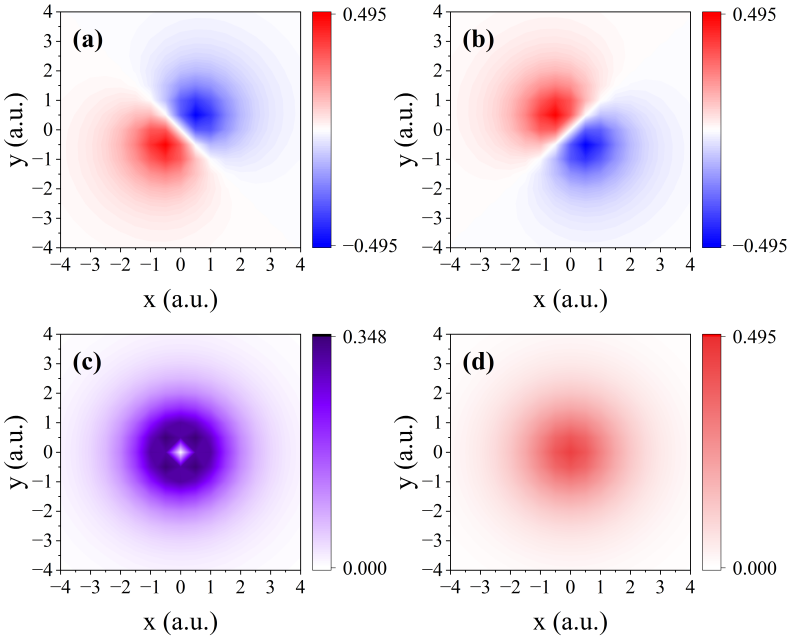


Figure 1. Initial states of argon. (**a**) Wave function of the p_x orbital. (**b**) Wave function of the p_y orbital obtained using the screened model potential in Equation (5). (**c**) Probability density (squared modulus) of the chiral current-carrying state p_+ defined by Equation (6). (**d**) Wave function of the 3*s* state calculated using the Coulomb model potential in Equation (4).

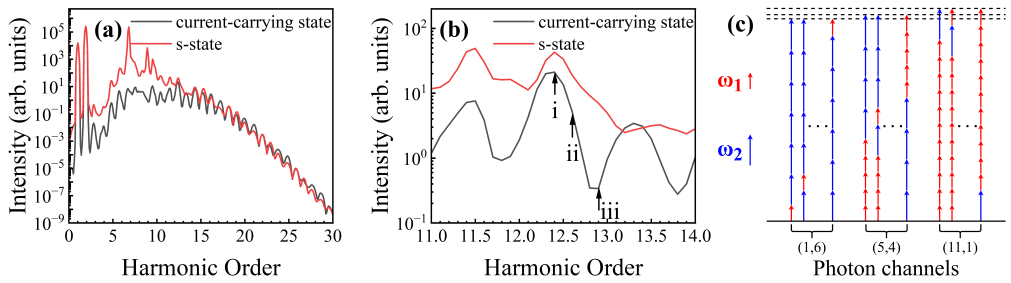


Figure 2. High-harmonic generation spectra from argon driven by a linearly polarized bichromatic vortex field. (**a**) Total HHG spectra calculated using the 3*s* state (black curve) and the p_+ state (red curve) as the initial states. (**b**) Enlarged view of harmonic orders 11–14. Three characteristic frequencies on the red curve are marked: (i) 12.4, (ii) 12.6, and (iii) 12.9. (**c**) Schematic illustration of the photon-channel concept. Specific harmonic orders arise from distinct quantum pathways defined by the absorption of n_1 and n_2 photons from the two field components.

The asymmetric double-lobe structure at the peak originates from the coupling between the linearly polarized bichromatic vortex field and the p_+ state, corresponding to the $(3p, m = +1)$ state. Although the probability density of this state is nearly isotropic, its complex wave function carries an intrinsic azimuthal probability current. The ionization dynamics are therefore governed not by geometric anisotropy, but by a nonadiabatic velocity-matching mechanism: ionization is enhanced when the intrinsic electron velocity is aligned with the instantaneous laser field and suppressed when it is misaligned. This

orientation-dependent effect acts as an angular gate and explains why the p_+ state produces a broken rotational symmetry in the harmonic intensity despite its nearly isotropic density distribution.

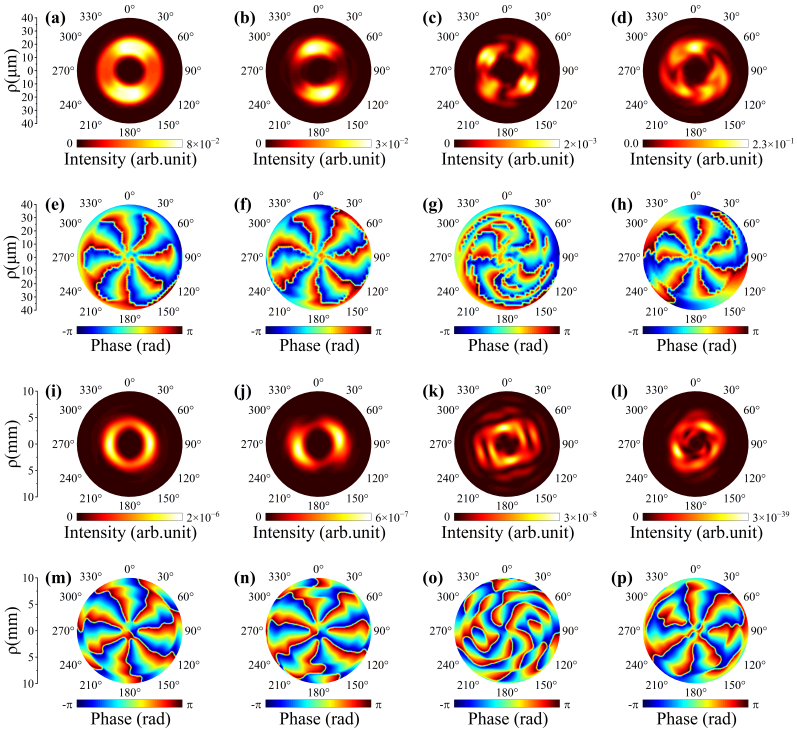


Figure 3. Near-field and far-field distributions of selected harmonic orders. (**a**–**c**) Near-field intensity distributions of harmonics at orders 12.4, 12.6, and 12.9 generated from the p_+ state. (**d**) Near-field intensity distribution of harmonic 12.4 generated from the 3*s* state. (**e**–**h**) Corresponding near-field phase distributions. (**i**–**l**) Far-field intensity distributions of the same harmonic orders. (**m**–**p**) Corresponding far-field phase distributions.

For comparison, the 12.4th-order harmonic generated from the isotropic 3*s* state exhibits a symmetric ring structure with arrow-like streamlines, as shown in Figure 3d. This is a characteristic feature of vortex-driven HHG. Its physical origin lies in the quantum probability current $\mathbf{j}$. Because the 3*s*-state wave function lacks an intrinsic azimuthal phase, the harmonic field driven by a vortex beam with topological charge ℓ can be written as $\psi \propto e^{i\ell\phi}R(\rho)$, giving rise to both azimuthal and radial current components. As a result, the local direction of energy flow varies continuously along the ring, producing the spiral intensity pattern.

The phase evolution across these frequencies provides direct evidence of photon-channel interference, as schematically illustrated in Figure 2c. Emission at a given frequency ω can arise from multiple quantum pathways, or photon channels, denoted by (n_1, n_2), where n_1 and n_2 are the numbers of photons absorbed from the two field components. When a specific channel (n_1, n_2) is spectrally matched to the selected emission frequency and also has favorable phase matching, it dominates the emission with a central frequency $\omega = (n_1 + 1.9n_2)\omega_1$ and a finite spectral width $\Delta\omega$. Because of this finite broadening, several channels can contribute simultaneously in the case of a noninteger frequency ratio, leading to spectral overlap.

At the 12.4th-order peak, the emission is dominated by the $(1, 6)$ photon channel. Here the emitted energy and the transferred OAM are determined by different combinations of the same photon numbers: the frequency is $\omega = (1 + 1.9 \times 6)\omega_1 = 12.4\omega_1$, whereas the OAM charge is $\ell = n_1\ell_1 + n_2\ell_2 = (1 + 6) \times 1 = 7$ because both driving components carry

$\ell_1 = \ell_2 = 1$. This well-defined OAM transfer gives rise to the clear seven-arm spiral phase pattern observed in Figure 3e. At the 12.6th-order shoulder, the local channel $(5, 4)$ becomes active, but the emission is still partially influenced by the spectral wing of the dominant $(1, 6)$ channel associated with the adjacent peak. Interference between these two pathways distorts the intensity into an asymmetric double-lobe pattern. It also perturbs the phase, producing a partially disordered seven-arm spiral. At the 12.9-order valley, the emission originates from the overlapping spectral tails of multiple channels. Interference between their incompatible OAM modes scrambles the wavefront, leading to a fully disordered phase and a fragmented four-lobe intensity distribution.

After propagation to the far field via Huygens' integral, the harmonic spatial modes preserve the essential characteristics of their near-field counterparts, as shown in Figure 3i–p. The peak retains a well-defined annular structure with clear spiral phase fronts, the shoulder remains asymmetric with a distorted phase, and the valley continues to display a fragmented intensity pattern accompanied by phase disorder. This near-to-far-field correspondence indicates that the observed modal features are imprinted at the generation stage rather than created by free-space propagation, and it enables direct comparison with experimentally measured far-field patterns.

3.2. Resolving Spectral Broadening and Topological Interference with a Counter-Rotating Bicircular Vortex Field

While the linearly polarized nondegenerate bichromatic field already reveals the transition from ordered to disordered harmonic modes, the spectral overlap between neighboring channels remains relatively strong. To resolve this process more clearly, we next consider a counter-rotating bicircular vortex field. Counter-rotating bicircular fields generate only $3n \pm 1$ harmonics because of the underlying C_3 symmetry [20], which produces a larger spectral separation between adjacent photon channels than in the nondegenerate 1:1.9 bichromatic case. As a result, the harmonic spectrum exhibits well-resolved discrete peaks, as shown in Figure 4a. This configuration therefore provides an ideal platform for resolving the spectral broadening of a single dominant channel and tracking its transition into interference regions with neighboring channels.

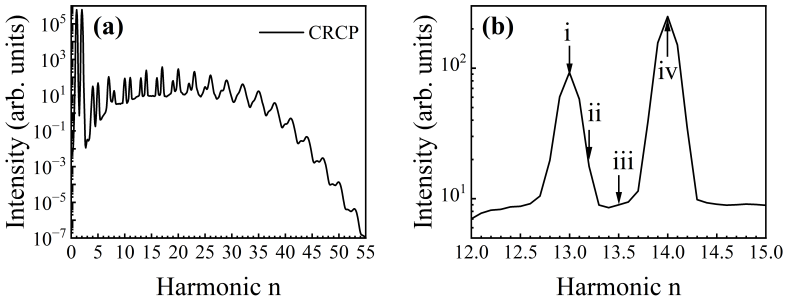


Figure 4. High-harmonic generation spectrum driven by a counter-rotating bicircular vortex field. (**a**) Total HHG spectrum. (**b**) Enlarged view of harmonic orders 12–15. Four characteristic frequencies are marked: (i) the 13th-order peak, (ii) the shoulder at 13.2, (iii) the valley at 13.5, and (iv) the 14th-order peak.

We examine harmonics from orders 12 to 15 in Figure 4b and select four characteristic frequencies: the 13th-order peak, the shoulder at 13.2, the valley at 13.5, and the 14th-order peak. Their near-field intensity and phase distributions are shown in Figure 5. At the dominant spectral peaks, the harmonics display symmetric annular intensity profiles and well-defined spiral phase structures. The nine-arm spiral pattern indicates single-channel

dominance. According to the OAM conservation law [21], the topological charge of the qth harmonic is

$$\ell_q = \left[\frac{q + 2\sigma_{q1}}{3}\right](\ell_1 + \ell_2) - \sigma_{q1}\ell_2, \tag{34}$$

where σ_{q1} denotes the helicity of the emitted harmonic component. For the 13th-order dominant channel $(5, 4)$ and the 14th-order channel $(4, 5)$, this relation gives $\ell = 9$ in both cases, but with opposite handedness. At the spectral shoulder, the phase distortion indicates the influence of spectral-wing contributions from neighboring pathways. In the valley region, strong phase disorder emerges from the overlap of counter-rotating channels, leading to destructive interference. The corresponding far-field patterns in Figure 5i–p preserve these main spatial features, further supporting the conclusion that the observed mode evolution originates from multi-channel interference in the source region rather than from propagation effects.

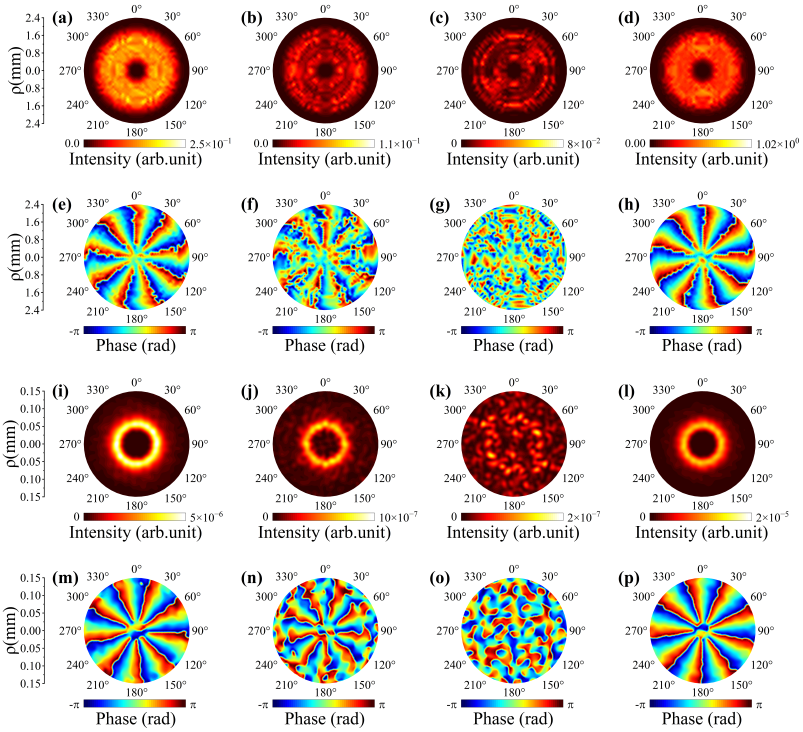


Figure 5. Near-field and far-field distributions of selected harmonic orders from the counter-rotating bicircular vortex field. (**a**–**d**) Near-field intensity distributions of harmonics at the characteristic frequencies marked in Figure 4b. (**e**–**h**) Corresponding near-field phase distributions. (**i**–**l**) Far-field intensity distributions of the same harmonics. (**m**–**p**) Corresponding far-field phase distributions.

This transition can also be quantified using the Stokes parameters. Based on near-field calculations, the harmonic peaks exhibit nearly pure circular polarization (13th order: DoP = 0.84, ellipticity $\epsilon = -0.998$; 14th order: DoP = 0.99, ellipticity $\epsilon = 1.000$), consistent with single-channel dominance. At the spectral shoulder, the DoP decreases to 0.15, indicating strong polarization mixing caused by the overlap of neighboring spectral wings. In the valley region, the DoP recovers to 0.64 while the ellipticity remains high ($\epsilon = 0.987$), showing that the field is not fully depolarized. Instead, it corresponds to an interference region where overlapping counter-rotating channels induce substantial phase and polarization modulation, while one helicity component remains dominant. This polarization evolution provides further evidence for the role of multi-channel interference.

3.3. OAM Spectrum and Microscopic Validation via Coherence Length

To further characterize the interference process, we analyze the OAM spectra at the four characteristic frequencies using the near-field harmonic emission. The results are shown in Figure 6. A clear selection rule is observed: only odd topological charges, such as $m = -11$, -9, and -7, exhibit substantial intensity, whereas even components remain negligible. This is consistent with OAM conservation in counter-rotating-bicircular-field-driven HHG [21]. The OAM spectra further indicate that the observed phase disorder does not originate from decoherence. Instead, it arises from vectorial interference between the overlapping spectral tails of the left-handed 13th and right-handed 14th harmonic channels. These channels share the same dominant OAM value, $\ell = -9$, but possess opposite spin states. Their coherent superposition forms a Poincaré-type polarization texture with spatially varying ellipticity, which generates local phase gradients while preserving the global OAM dominance at $\ell = -9$.

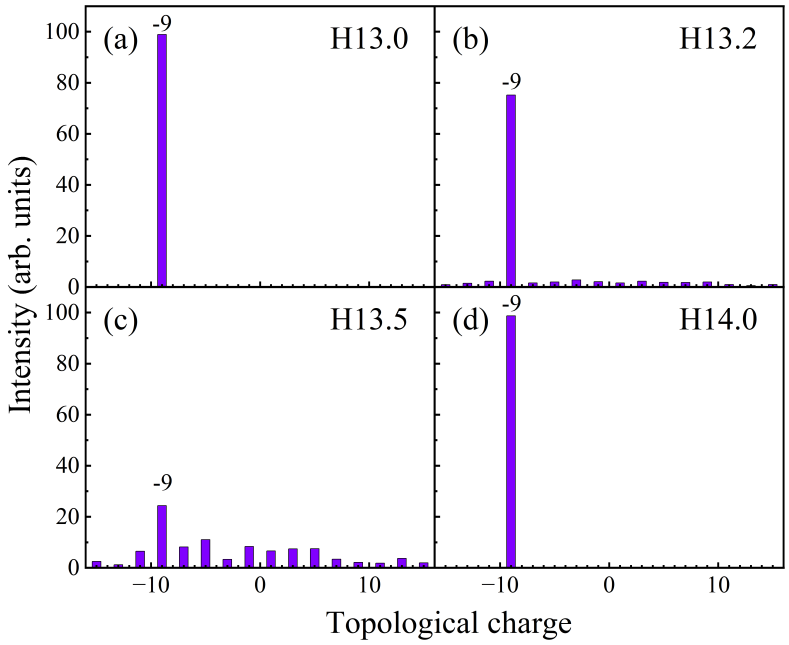


Figure 6. OAM spectral decomposition for the harmonics analyzed in the counter-rotating bicircular vortex field. The normalized OAM spectra are shown for the four characteristic frequencies: (**a**) the 13th-order peak, (**b**) order 13.2, (**c**) order 13.5, and (**d**) the 14th-order peak.

The combined evolution of spatial phase disorder, polarization transition from circular to elliptical, and preserved OAM dominance demonstrates that the spectral valleys are not empty regions of suppressed emission, but rather structured interference domains produced by the coherent overlap of broadened photon channels.

To elucidate the microscopic origin of the observed spatial modes, we analyze the phase mismatch and transverse coherence length across the spectral peak, shoulder, and valley, as shown in Figure 7a–f. At the dominant spectral peak (12.4th order), the phase-mismatch map in Figure 7a exhibits a broad plateau near zero in the central region, surrounded by an ordered spiral structure. Correspondingly, the transverse coherence length is high, exceeding 300 μm in Figure 7d, and forms a robust annular region of high coherence that spatially overlaps with the bright lobes in Figure 3b. In the shoulder region (12.6th order), the phase mismatch evolves into a distinct two-arm spiral pattern (Figure 7b), reflecting interference between the dominant quantum pathway $(1, 6)$ and the emerging pathway $(5, 4)$. As a consequence, the coherence length decreases to 100–200 μm (Figure 7e), causing

the coherence ring to fragment. At the spectral valley (12.9th order), the phase mismatch becomes highly disordered and speckled (Figure 7c). The coherence length correspondingly drops to below 10 μm (Figure 7f), accounting for the diffuse spatial profile.

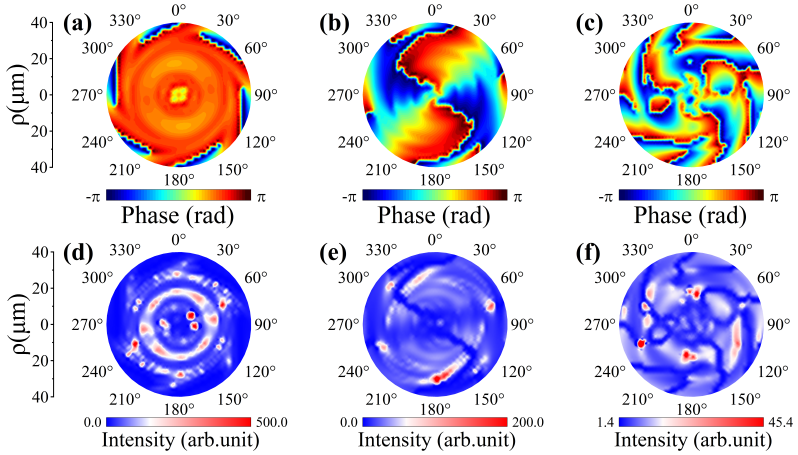


Figure 7. Phase mismatch and transverse coherence-length analysis for harmonics generated by the linearly polarized field. (**a**–**c**) Spatial maps of the phase mismatch for harmonics at orders 12.4, 12.6, and 12.9, respectively. (**d**–**f**) Corresponding spatial maps of the transverse coherence length.

These results establish a direct connection between microscopic quantum-path interference and macroscopic spatial mode. In this sense, the transverse coherence length acts as an effective filter for spectrally broadened channels, driving the transition from coherent spatial localization at intensity maxima to stochastic divergence in spectral minima.

4. Conclusions

In conclusion, our OAM-resolved framework provides a physical picture of how photon-channel interference governs the spatial-mode evolution of high-order harmonics driven by bichromatic vortex fields. In particular, the evolution of the harmonic spatial mode serves as a signature of the transition from single-channel to multi-channel dominance, a process controlled by finite spectral broadening. This interference mechanism enables control of the harmonic OAM, polarization state, and transverse spatial coherence, while maintaining high spatial coherence (exceeding 100 μm) at spectral peaks. Because such coherence can be comparable to or larger than characteristic microscopic material length scales, the present source-mode and OAM-channel analysis may provide a useful basis for future extensions to structured-light probes of topological materials. More broadly, this work establishes a field-control framework that links strong-field vortex-driven HHG with OAM-resolved structured-light applications, while a direct calculation of material-specific topological observables is left for future work.

Author Contributions: Conceptualization, Z.-J.X.; methodology, J.G.; software, J.G.; validation, Z.-J.X. and R.-Y.Z.; formal analysis, Z.-J.X.; investigation, Z.-J.X.; resources, J.G.; data curation, Z.-J.X.; writing—original draft preparation, Z.-J.X.; visualization, R.-Y.Z.; writing—review and editing, Z.-J.X., R.-Y.Z. and J.G.; supervision, J.G. All authors have read and agreed to the published version of the manuscript.

Funding: This research was funded by the National Natural Science Foundation of China, grant number 12074146, and the Natural Science Foundation of Jilin Province, grant number 20220101010JC.

Data Availability Statement: The data that support the findings of this study are available from the corresponding author upon reasonable request.

Conflicts of Interest: The authors declare no conflicts of interest.

References

1. McPherson, A.; Gibson, G.; Jara, H.; Johann, U.; Luk, T.S.; McIntyre, I.A.; Boyer, K.; Rhodes, C.K. Studies of multiphoton production of vacuum-ultraviolet radiation in the rare gases. *J. Opt. Soc. Am. B* **1987**, *4*, 595–601. [CrossRef]
2. Ferray, M.; L'Huillier, A.; Li, X.F.; Lompré, L.A.; Mainfray, G.; Manus, C. Multiple-harmonic conversion of 1064 nm radiation in rare gases. *J. Phys. B* **1988**, *21*, L31. [CrossRef]
3. Corkum, P.B. Plasma perspective on strong field multiphoton ionization. *Phys. Rev. Lett.* **1993**, *71*, 1994–1997. [CrossRef] [PubMed]
4. Hentschel, M.; Kienberger, R.; Spielmann, C.; Reider, G.A.; Milosevic, N.; Brabec, T.; Corkum, P.; Heinzmann, U.; Drescher, M.; Krausz, F. Attosecond metrology. *Nature* **2001**, *414*, 509–513. [CrossRef] [PubMed]
5. Mauritsson, J.; Johnsson, P.; Gustafsson, E.; L'Huillier, A.; Schafer, K.J.; Gaarde, M.B. Attosecond pulse trains generated using two color laser fields. *Phys. Rev. Lett.* **2006**, *97*, 013001. [CrossRef] [PubMed]
6. Bertrand, J.B.; Wörner, H.J.; Bandulet, H.C.; Bisson, E.; Spanner, M.; Kieffer, J.C.; Villeneuve, D.M.; Corkum, P.B. Ultrahigh-order wave mixing in noncollinear high harmonic generation. *Phys. Rev. Lett.* **2011**, *106*, 023001. [CrossRef] [PubMed]
7. Li, L.; Lan, P.; He, L.; Zhu, X.; Chen, J.; Lu, P. Scaling law of high harmonic generation in the framework of photon channel. *Phys. Rev. Lett.* **2018**, *120*, 223203. [CrossRef] [PubMed]
8. Allen, L.; Beijersbergen, M.W.; Spreeuw, R.J.C.; Woerdman, J.P. Orbital angular momentum of light and transformation of Laguerre–Gaussian laser modes. *Phys. Rev. A* **1992**, *45*, 8185–8189. [CrossRef] [PubMed]
9. Zürch, M.; Kern, C.; Hansinger, P.; Dreischuh, A.; Spielmann, C. Strong-field physics with singular light beams. *Nat. Phys.* **2012**, *8*, 743–746. [CrossRef]
10. Hernández-García, C.; Picón, A.; Román, J.S.; Plaja, L. Attosecond extreme ultraviolet vortices from high-order harmonic generation. *Phys. Rev. Lett.* **2013**, *111*, 083602. [CrossRef] [PubMed]
11. Gariepy, G.; Leach, J.; Kim, K.T.; Hammond, T.J.; Frumker, E.; Boyd, R.W.; Corkum, P.B. Creating high-harmonic beams with controlled orbital angular momentum. *Phys. Rev. Lett.* **2014**, *113*, 153901. [CrossRef] [PubMed]
12. Géneaux, R.; Camper, A.; Auguste, T.; Gobert, O.; Caillat, J.; Taïeb, R.; Ruchon, T. Synthesis and characterization of attosecond light vortices in the extreme ultraviolet. *Nat. Commun.* **2016**, *7*, 12583. [CrossRef] [PubMed]
13. Kong, F.; Zhang, C.; Bouchard, F.; Li, Z.; Brown, G.G.; Ko, D.H.; Hammond, T.J.; Arissian, L.; Boyd, R.W.; Karimi, E.; et al. Controlling the orbital angular momentum of high harmonic vortices. *Nat. Commun.* **2017**, *8*, 14970. [CrossRef] [PubMed]
14. Gauthier, D.; Rebernik Ribič, P.; Adhikary, G.; Camper, A.; Chappuis, C.; Cucini, R.; DiMauro, L.F.; Dovillaire, G.; Frassetto, F.; Géneaux, R.; et al. Tunable orbital angular momentum in high-harmonic generation. *Nat. Commun.* **2017**, *8*, 14971. [CrossRef] [PubMed]
15. Wang, Z.; Hong, W.; Wang, F.; Liao, Q. Tuning the orbital angular momentum of high harmonics by manipulating the collinear photon channels in two-color high-harmonic generation. *Phys. Rev. Res.* **2020**, *2*, 033482. [CrossRef]
16. Feit, M.D.; Fleck, J.A.; Steiger, A. Solution of the Schrödinger equation by a spectral method. *J. Comput. Phys.* **1982**, *47*, 412–433. [CrossRef]
17. Jin, C.; Li, B.; Wang, K.; Xu, C.; Lin, C.D. Phase-matching analysis in high-order harmonic generation with nonzero orbital angular momentum Laguerre–Gaussian beams. *Phys. Rev. A* **2020**, *102*, 033113. [CrossRef]
18. Gaarde, M.B.; Tate, J.L.; Schafer, K.J. Macroscopic aspects of attosecond pulse generation. *J. Phys. B* **2008**, *41*, 132001. [CrossRef]
19. Eckart, S.; Kunitski, M.; Richter, M.; Hartung, A.; Rist, J.; Trinter, F.; Fehre, K.; Schlott, N.; Henrichs, K.; Schmidt, L.; et al. Ultrafast preparation and detection of ring currents in single atoms. *Nat. Phys.* **2018**, *14*, 701–704. [CrossRef]
20. Liu, X.; Zhu, X.; Li, L.; Li, Y.; Zhang, Q.; Lan, P.; Lu, P. Selection rules of high-order-harmonic generation: Symmetries of molecules and laser fields. *Phys. Rev. A* **2016**, *94*, 033410. [CrossRef]
21. Dorney, K.M.; Rego, L.; Brooks, N.J.; San Rom'an, J.; Liao, C.T.; Ellis, J.L.; Zusin, D.; Gentry, C.; Nguyen, Q.L.; Shaw, J.M.; et al. Controlling the polarization and vortex charge of attosecond high-harmonic beams via simultaneous spin–orbit momentum conservation. *Nat. Photonics* **2019**, *13*, 123–130.

Disclaimer/Publisher's Note: The statements, opinions and data contained in all publications are solely those of the individual author(s) and contributor(s) and not of MDPI and/or the editor(s). MDPI and/or the editor(s) disclaim responsibility for any injury to people or property resulting from any ideas, methods, instructions or products referred to in the content.